High Performance Algorithms for Global BRDF Retrieval *

Zengyan Zhang[1] Satya Kalluri[2] Joseph JáJá[1]
Shunlin Liang[2] John Townshend[3]

Institute for Advanced Computer Studies (UMIACS)
University of Maryland, College Park, MD 20742
July 22, 1997

Abstract

Most Land cover types are "anisotropic", that is, the solar radiation reflected by the surface is not uniform in all directions. Characterizing the *Bidirectional Reflectance Distribution Function* (BRDF) of the earth's surface is critical in understanding surface anisotropy. Though there are several methods to retrieve the BRDF of various land cover types, most of them have been applied over small data sets collected either on ground or from aircraft at limited spatial and temporal scales.

In this paper, we use multi-angular, multi-temporal and multi-band Pathfinder AVHRR Land (PAL) data set to retrieve the **global** BRDF in the red and near infrared wavelengths. The PAL data set used in our study has a spatial resolution of 8-km and 10-day composite data for four years (1983 to 1986). In particular, we develop high performance algorithms to retrieve global BRDF using three widely different models. Given the volume of data involved (about 27 GBytes), we attempt to optimize the I/O time as well as minimize the overall computational complexity. Our algorithms access the global data once, followed by a redistribution of land pixel data to balance the computational loads among the different nodes of a multiprocessor system. This strategy results in an optimized I/O access time with efficiently balanced computations across the nodes. Experimental data on a 16-node IBM SP2 is used to support these claims and to illustrate the scalability of our algorithms.

Keywords: High Performance Computing, Remote Sensing, Bidirectional Reflectance Distribution Function (BRDF), Advanced Very High Resolution Radiometer (AVHRR), Pathfinder AVHRR Land data set (PAL)

---

[1] UMIACS and Department of Electrical Engineering
[2] Department of Geography
[3] UMIACS and Department of Geography

1 Introduction

At regional scales, satellite-based sensors are the primary source of information to study the earth's system science, as they provide the needed dynamic temporal view of the earth's surface. Surface reflectance measurements from satellite data have been widely used to detect land cover change [1], surface albedo and energy budget [2], seasonal and inter-annual vegetation dynamics [3], and to derive biophysical parameters [4, 5] . However, the spectral measurements taken by most of the existing sensor systems (e.g. Advanced Very High Resolution Radiometer (AVHRR)) are directional. Because most land cover types are "anisotropic", these observations (e.g. reflectance) are valid only for a particular sensor-illumination geometry. Land surface anisotropy causes variations in surface reflectances when measured under different illumination and view angles. The *Bidirectional Reflectance Distribution Function* (BRDF) of the surface $(f_r(\theta_v, \theta_s, \phi_v, \phi_s, \lambda))$ specifies the behavior of the surface scattering as a function of illumination and viewing angles at particular wavelengths, and can be written as:

$$f_r(\theta_v, \theta_s, \phi_v, \phi_s, \lambda) = \frac{\partial L_v(\theta_v, \theta_s, \phi_v, \phi_s, \lambda, E_i)}{\partial E(\theta_s, \phi_s, \lambda)} \tag{1}$$

where θ, ϕ, and λ are the zenith and azimuth angles, and wavelength respectively [6]. The subscript v denotes sensor and s denotes the sun respectively. "L_v" is the reflected radiance in the view direction measured by the sensor and "E" is the parallel beam irradiance from the illumination direction in the wave band. Note that $f_r(\theta_v, \theta_s, \phi_v, \phi_s, \lambda)$ has the unit sr^{-1} (sr means steradian). To make BRDF directly comparable to bidirectional surface reflectance and hemispherical reflectance, we refer to BRDF as $\rho = f_r \pi$. [7]

1.1 Why is it important to understand BRDF?

For several radiative transfer and energy balance studies of the land surface we need the surface reflectance that is integrated over all viewing angles in the upward hemisphere ("hemispherical reflectance"), and over the visible and near-infrared wavelength, which is called as the "broad band albedo". The albedo of a surface describes the ratio of radiant energy scattered upward and away from the surface in all directions to the down-welling irradiance incident upon the surface. The hemispherical spectral reflectance $(\rho_h(\theta_s, \lambda))$ is described by:

$$\rho_h(\theta_s, \lambda) = \frac{1}{\pi} \int_0^{2\pi} \int_0^{\frac{\pi}{2}} \rho(\theta_s, \theta_v, \phi, \lambda) \cos\theta_v \sin\theta_v d\theta_v d\phi \tag{2}$$

where $\rho(\theta_s, \theta_v, \phi, \lambda)$ is the surface BRDF, and ϕ is the relative azimuth angle ($\phi = \phi_v - \phi_s$). When the equation is integrated over all possible solar zenith angles (θ_s), it is known as the bi-hemispherical reflectance.

Another important reason for understanding the surface BRDF is due to the fact that vegetation indices (e.g. Normalized Difference Vegetation Index (NDVI)) which are derived from a combination of spectral bands are also effected by the surface BRDF. Thus, understanding the surface BRDF will allow us [7]

- To correct multi-date images taken at different view angles for BRDF effects (e.g. in creation of temporal composites).

- To retrieve surface structural attributes (e.g. leaf area index and biomass) and land cover information from the scattering behavior of the surface.

- To accurately retrieve broad band albedo required for energy balance and radiative transfer studies.

The BRDF of land surface at the top of the atmosphere is different from the BRDF measured at the surface because of atmospheric effects. However studies [8, 9] have shown that the net shortwave energy balance retrieved at the top of the atmosphere (TOA) is linear and directly proportional to the net shortwave fluxes measured on the ground. Thus, the albedo and BRDF retrieved at the top of atmosphere could still be used in energy balance studies.

1.2   How to compute BRDF?

The BRDF models can be broadly classified into physically based models, empirical models and semi-empirical models. Physically based models include geometric-optical models [10], turbid medium models [11, 12], hybrid models [13] and computer simulation models [14, 15, 16]. The physical models are complex, computationally demanding and, thus far, these models have only been developed for specific land cover types, with no known universal models for different cover types. These models are dependent upon the structural and state attributes of the land surface such as the leaf angle distribution on plant canopies, photo-synthetic activity, shape and size of plants (e.g. cylindrical, spherical, conical) etc. The development and application of these physical based models have been limited to BRDF modeling activities.

The empirical models are simple to use and have been applied fairly widely, although the model coefficients may not have a physical meaning. One of the most widely used empirical model is that of Modified Walthall model [17], expressed as:

$$\rho(\theta_s, \theta_v, \phi, \lambda) = a_0(\theta_v^2 + \theta_s^2) + a_1\theta_v^2\theta_s^2 + a_2\theta_v\theta_s \cos\phi + a_3 \tag{3}$$

where a_{0-3} are the parameters of the model.

Semi-empirical models try to provide the balance between the physically providing empirical coefficients that have a physical meaning. One of the models that has been

successfully tested is that of Rahman et al. [18], which describes the surface BRDF as:

$$\rho(\theta_s, \theta_v, \phi, \lambda) = \rho_0(\cos\theta_v \cos\theta_s(\cos\theta_v + \cos\theta_s))^{k-1}F(g)[1 + R(G)] \qquad (4)$$

where

$$
\begin{aligned}
F(g) &= \frac{1 - \Theta^2}{[1 + \Theta^2 - 2\Theta\cos(\pi - g)]^{\frac{3}{2}}} \\
\cos g &= \cos\theta_s \cos\theta_v + \sin\theta_s \sin\theta_v \cos\phi \\
1 + R(G) &= 1 + \frac{1 - \rho_0}{1 + G} \\
G &= [\tan^2\theta_v + \tan^2\theta_s - 2\tan\theta_v \tan\theta_s \cos\phi]^{\frac{1}{2}}
\end{aligned}
$$

In the above set of equations there are three unknown parameters ρ_0, k and Θ which have to be determined by model inversion and numerical iteration.

The above models assume that the variations in surface reflectance are caused by changes in viewing and illumination geometry only. When we fit angular models to multitemporal observations, we hope to get longer records in order to get enough angular sampling. It is assumed that the target does not change significantly over the period of the measurements. However, many cover types have seasonal or annual changes. For example, pixel of an agricultural land could correspond to a dense canopy in the growing season and a bare soil in the winter season. Canopies have quite different angular behavior from soils.

The long term record of AVHRR observations provides an excellent opportunity to explore the angular signatures based on the multitemporal data assembly approach. The long time series are sufficient to link bidirectional reflectance with surface characteristics through different modeling approaches. However, almost all empirical or semi-empirical models do not take account of temporal variations. In this study, a temporal angular model is developed in which a temporal component is approximated by a Fourier series and an angular component is expressed by the modified Walthall model. It describes surface BRDF as follows:

$$
\begin{aligned}
\rho(\theta_s, \theta_v, \phi, \lambda) = {}& a_0(\theta_v^2 + \theta_s^2) + a_1\theta_v^2\theta_s^2 + a_2\theta_v\theta_s\cos\phi + a_3 \\
& + a_4\cos(\frac{2\pi t}{N}) + a_5\sin(\frac{2\pi t}{N}) + a_6\cos(\frac{4\pi t}{N}) + a_7\sin(\frac{4\pi t}{N}) \quad (5)
\end{aligned}
$$

where N is the number of data points for each year, and t varies from 0 to $N - 1$. This model has been compared with some other empirical models and gives the best fit to all data points from PAL data set [19].

2 Global BRDF Retrieval Computational Approach

We use Pathfinder AVHRR Land (PAL) data set and the three models described above to derive the global BRDF. Our overall Computational approach is outlined
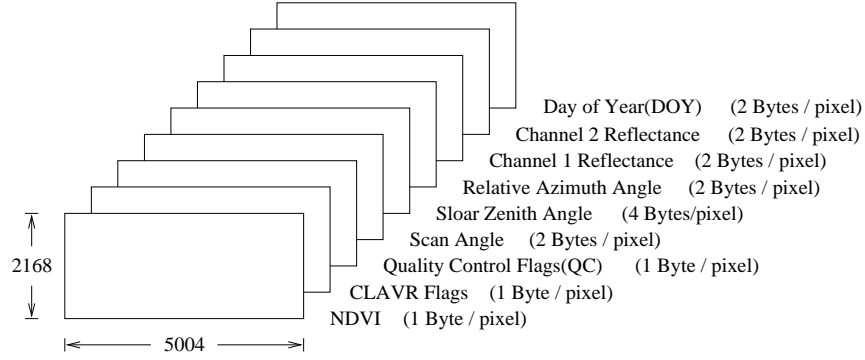
Figure 1: Layout of the Pathfinder AVHRR Land 10-day composite data set that was used as input to derive the BRDF parameters (11 million pixels/image, 9 layers)

next.

The input consists of four years $(1983 - 1986)$ of PAL data set that has a spatial resolution of 8-km with a 10-day composite [20]. Although PAL data set spans from 1981 to 1994, we only choose these 4 years of data because the data from the other years has processing errors. There are 36 10-day composite data for each year, and we use 9 data layers out of 12 layers from each composite, as shown in Figure 1. For our application, we make use of three types of information available for each pixel of the composite images:

- Pixel selection information based on the values of the flags QC (data valid or not) and CLAVR (pixel clear, mixed or cloudy).

- Temporal and geometric information based on the values in the layers DOY, Sensor Scan Angle, Solar Zenith Angle, Relative Azimuth Angle and the reflectance values in channels 1 and 2.

- Validation information: The PAL data set also contains the NDVI which is derived from channel $1(\rho_{ch1})$ and $2(\rho_{ch2})$ reflectance measurements of AVHRR:

$$NDVI = \frac{\rho_{ch2} - \rho_{ch1}}{\rho_{ch2} + \rho_{ch1}} \qquad (6)$$

We recompute the NDVI for each pixel from ρ_{ch1}, ρ_{ch2} estimated by each of the BRDF models, and compare it with the NDVI value reported in the PAL data set for validation. Spatial and temporal variations in NDVI from AVHRR have been shown to be correlated with phenology of land cover [21]. The mean and standard deviation of NDVI for each pixel are used to determine how the surface is changing over the curve fitting period.

For each pixel, we derive the coefficients required to describe the surface BRDF by linear least squares fit for the linear BRDF models, and by model inversion and iteration for the non-linear model. For every pixel, the coefficients a_i (i from 1 to N_c) for channels 1 and 2 are generated for each model. In addition, some statistical information on the model fit will be provided to allow a more in-depth analysis. In particular, we compute the following quantities:

- The standard error of channel 1 and 2, which provides a quantitative measure on the goodness of the model fit.

- For the linear models, the regression analysis coefficient R^2, which is the ratio of the variance of the predicted data and the variance of the given data. The coefficient R^2 shows how well the model fit the given data and indicates the proportion of the variation "explained" by the regression line [22].

- The standard error between NDVI in the PAL data set and the NDVI estimated by each BRDF model.

- The mean and standard deviation of NDVI in the PAL data set to study the changes on the land surface over the time period.

3   Pixel Computation

In this section, we describe the computation that takes place at each pixel, and include an estimate of the number of operations required per pixel. In the following analysis, N_d represents the number of data points used for the model fitting and k represents the number of floating point operations needed to evaluate a trigonometric function such as sin, cos or arcsin. In practice $k \approx 25$, and we assume that the time required to perform the floating point multiplication and addition/subtraction are the same.

3.1   Input Data Conditioning

When the PAL data set was generated, the physical values were scaled to an appropriate 8-bit (unsigned) or 16-bit (unsigned) integer value (Figure 1) as detailed in [23]. We need to re-scale the PAL input data back to floating point data for our application, convert solar zenith angle (from degree to radian), and sensor scan angle (to the view zenith angle). To condition the input, we need $N_d(27+3k)$ floating point operations per pixel.

3.2   Linear BRDF Model

As we have seen in Section 1, the linear BRDF model can be expressed as follows:

$$\rho(\theta_s, \theta_v, \phi, \lambda) = \sum_{i=1}^{N_c} a_i f_i(\theta_s, \theta_v, \phi, \lambda) \tag{7}$$

where N_c is the number of coefficients for the model, the a_i's are the model coefficients, θ_s, θ_v, ϕ are the solar zenith angle, view zenith angle, and relative azimuth angle respectively. Taking channel 1 as an example, the BRDF model fitting problem can be expressed as follows:

> Given a set of data values $(\theta_s^j, \theta_v^j, \phi^j, \rho_1^j), j = 1, 2, \ldots N_d$ and the BRDF model equation(7), choose the linear model coefficients that best describe the function relationship between ρ_1 and the independent variables θ_s, θ_v and ϕ

For the least squares method [24, 25], the "best" coefficients a_i (i from 1 to N_c) are chosen to minimize the cumulative error between the given value ρ_1^j and the model predicated value $\hat{\rho}_1^{\,j}$. The cumulative error is defined as follows:

$$\sum_{j=1}^{N_d} (\rho_1^j - \hat{\rho}_1^{\,j})^2 = \sum_{j=1}^{N_d} (\rho_1^j - \sum_{i=1}^{N_c} a_i f_i(\theta_s^j, \theta_v^j, \phi^j))^2 \tag{8}$$

Clearly, the function of Eqn.(7) has continuous partial derivatives in terms of the model coefficients a_i, so we can get a necessary condition for the the "best" coefficients a_i (i from 1 to N_c) as follows:

$$\frac{\partial}{\partial a_i} \sum_{j=1}^{N_d} (\rho_1^j - \sum_{i=1}^{N_c} a_i f_i(\theta_s^j, \theta_v^j, \phi^j))^2 = 0 \qquad i = 1, 2, \ldots, N_c \tag{9}$$

Simplifying, we obtain the following normal equations:

$$\sum_{k=1}^{N_c} a_k \sum_{j=1}^{N_d} f_i(\theta_s^j, \theta_v^j, \phi^j) f_k(\theta_s^j, \theta_v^j, \phi^j) = \sum_{j=1}^{N_d} \rho_1^j f_i(\theta_s^j, \theta_v^j, \phi^j) \qquad i = 1, 2, \ldots N_c \tag{10}$$

Similarly, we can get the normal equations for channel 2 as follows:

$$\sum_{k=1}^{N_c} a_k \sum_{j=1}^{N_d} f_i(\theta_s^j, \theta_v^j, \phi^j) f_k(\theta_s^j, \theta_v^j, \phi^j) = \sum_{j=1}^{N_d} \rho_2^j f_i(\theta_s^j, \theta_v^j, \phi^j) \qquad i = 1, 2, \ldots N_c \tag{11}$$

The normal equations(10) and (11) can be expressed as a linear system

$$\mathbf{A}^T \mathbf{A} \mathbf{a} = \mathbf{A}^T \mathbf{y} \tag{12}$$

7

where

$$\mathbf{A} = \begin{bmatrix} f_1(\theta_s^1, \theta_v^1, \phi^1) & f_2(\theta_s^1, \theta_v^1, \phi^1) & \ldots & f_{N_c}(\theta_s^1, \theta_v^1, \phi^1) \\ f_1(\theta_s^2, \theta_v^2, \phi^2) & f_2(\theta_s^2, \theta_v^2, \phi^2) & \ldots & f_{N_c}(\theta_s^2, \theta_v^2, \phi^2) \\ \vdots & \vdots & & \vdots \\ f_1(\theta_s^{N_d}, \theta_v^{N_d}, \phi^{N_d}) & f_2(\theta_s^{N_d}, \theta_v^{N_d}, \phi^{N_d}) & \ldots & f_{N_c}(\theta_s^{N_d}, \theta_v^{N_d}, \phi^{N_d}) \end{bmatrix}$$

$$\mathbf{a} = \begin{bmatrix} a_{11} & a_{21} \\ a_{12} & a_{22} \\ \vdots & \vdots \\ a_{1N_c} & a_{2N_c} \end{bmatrix} \qquad \mathbf{y} = \begin{bmatrix} \rho_1^1 & \rho_2^1 \\ \rho_1^2 & \rho_2^2 \\ \vdots & \vdots \\ \rho_1^{N_d} & \rho_2^{N_d} \end{bmatrix}$$

$(\theta_s^j, \theta_v^j, \phi^j, \rho_1^j, \rho_2^j)$ $(j = 1, 2, \ldots N_d)$ are the data points. ρ_1, ρ_2 are reflectances of channel 1 and 2 respectively. a_{1j} and a_{2j} (j from 1 to N_c) are the coefficients for channel 1 and 2 respectively. We can solve this linear system by Gaussian elimination followed by a backward substitution.

To form the normal equations, we need to evaluate the functions $f_i(\theta_s, \theta_v, \phi, \lambda)$ for the given points. The number of floating point operations needed to determine these functions depends on the model used. Suppose the evaluation of the f_i's at a single point requires F_f FLOPs. Then to form the normal equations we need $N_d(F_f + N_c^2 + 5N_c)$ operations using the symmetric properties of the left hand side $\mathbf{A}^T\mathbf{A}$ of Eqn.(12).

Gaussian elimination followed by a backward substitution for the linear system in Eqn.(12) will require about $\frac{2N_c^3}{3} + \frac{5N_c^2}{2} + \frac{11N_c}{6}$ FLOPs. Hence, we need $\frac{2N_c^3}{3} + \frac{5N_c^2}{2} + \frac{11N_c}{6} + N_d(F_f + N_c^2 + 5N_c)$ FLOPs per pixel.

3.3 Non-linear BRDF Model

For Rahman's model, we need a non-linear least squares fit. The non-linear model can be written as $\rho = f(\mathbf{a}, \theta_v, \theta_s, \phi, \lambda)$, where $\mathbf{a}$ is the model coefficient vector. In particular, $\mathbf{a} = [\rho_o, k, \Theta]^T$ for Rahman's model. As in the case of linear least squares fit, we aim at minimizing the cumulative squared error for each channel. Taking channel 1 for example, the cumulative error is:

$$J(\mathbf{a}) = \sum_{j=1}^{N_d} (\rho^j - f(\mathbf{a}, \theta_v^j, \theta_s^j, \phi^j))^2 \tag{13}$$

We can minimize this error using the Powell's method [26, 27]. The basic idea here is to change the multidimensional minimization problem to a sequence of line minimizations, which minimizes the function $J(\mathbf{a})$ along some vector direction $\mathbf{n}$ using one dimensional methods. Powell's algorithm can be described as follows [26]:

Let $\mathbf{a}_0$ be an initial guess of the coefficients and let $\mathbf{u}_i$ (i from 1 to N_c) be the N_c-dimensional basis vector, i.e. $\mathbf{u}_i = \mathbf{e}_i$. Then repeat the following steps until the function $J(\mathbf{a})$ stops decreasing:

- Save starting point as $\mathbf{a}_0$

- For $i = 1, 2, \ldots N_c$, compute λ_i which minimizes $J(\mathbf{a}_{i-1} + \lambda_i \mathbf{u}_i)$ and call this point $\mathbf{a}_i$

- For $i = 1, 2, \ldots N_c - 1$, replace $\mathbf{u}_i$ by $\mathbf{u}_{i+1}$

- Replace $\mathbf{u}_{N_c}$ by $\mathbf{a}_{N_c} - \mathbf{a}_0$

- Compute λ that minimize $J(\mathbf{a}_0 + \lambda \mathbf{u}_{N_c})$ and call this point $\mathbf{a}_0$.

The line minimization problem can be expressed as follows [27]:

Given the input vector $\mathbf{a}$, *the direction vector* $\mathbf{n}$ *and the function* $J(\mathbf{a})$, *find the scalar* λ *that minimizes* $J(\mathbf{a} + \lambda \mathbf{n})$. *Replace* $\mathbf{a}$ *by* $\mathbf{a} + \lambda \mathbf{n}$, *and* $\mathbf{n}$ *by* $\lambda \mathbf{n}$.

We can change the multi-dimensional function $J(\mathbf{a})$ along the line going through $\mathbf{a}$ in the direction $\mathbf{n}$ to a one dimensional function $J_1(\lambda)$ [27]. That is, we first evaluate $(\mathbf{a} + \lambda \mathbf{n})$, and then compute the function value of the original function. Hence we can think of J_1 as a function of λ.

To solve such a one dimensional line minimization problem, we first bracket the minimum along this line. We know that a minimum is bracketed only when there is a triplet of points, $a < b < c$, such that $J_1(b)$ is less than both $J_1(a)$ and $J_1(c)$. In this case, we know that the function $J_1(\lambda)$ has a minimum in the interval (a, c). We can start with some initial guess as left point of the bracketing triplet and then step downhill to find the middle point of the bracketing triplet. The middle point can be found by increasing the step size either by a constant factor, or else by the result of a parabolic extrapolation to the preceding points that is designed to take us to the extrapolated turning point [27]. Then we just need to take a big enough step to stop the downhill trend and get a high third point.

We can then solve the the line minimization problem using Brent's method [26]. The basic idea is to use parabolic interpolation. Given three points $(a, J_1(a))$, $(b, J_1(b))$, $(c, J_1(c))$, the formula for the abscissa x that is the minimum of a parabola through these three points is

$$x = b - \frac{1}{2} \frac{(b-a)^2 [J_1(b) - J_1(c)] - (b-c)^2 [J_1(b) - J_1(a)]}{(b-a)[J_1(b) - J_1(c)] - (b-c)[J_1(b) - J_1(a)]}$$

But using this formula solely is not likely to succeed in practice. Brent's method keeps track of 6 function points and can solve the task in all the cases. For a detailed discussions, see [26, 27].

Operation Counts for Rahman's Model: Let I_1 be the number of iterations to bracket the minimum in the line minimization part, I_2 be the number of iterations required in Brent's method and I_3 be the number of iterations needed by Powell's method. For each iteration in Powell's method, we need to do $(N_c + 1)$ line minimizations and evaluate the error function $J(\mathbf{a})$ once, plus some other memory and

9

bookkeeping operations. In our case, we have that $N_d = 25$, $N_c = 3$, $I_1 = 3$, $I_2 = 18$ and $I_3 = 22$ on average. Hence, we need 3.9 MFLOPs per pixel to do the non-linear least squares fit for the Rahman's model.

3.4 Model Verification Information Generation

Using the model coefficients generated, we compute the reflectances for channels 1 and 2, and then the NDVI values as stated in Eqn.(6). Here we need to compute the channel reflectance, NDVI mean and standard error, channel 1 and 2 standard error, R^2. Overall, we will need $N_d(2N_c + 22)$ FLOPs per pixel to perform these computations.

4 High Performance Algorithms for Global BRDF Retrieval

4.1 Initial Data Layout

Given the large amounts of data involved (about 27 GBytes) and the large computational requirements per pixel, we develop an implementation on a multi-processor system, where each node has a sufficiently large storage subsystem. The implementation on other multiprocessor configurations is similar. For global BRDF retrieval, the main goal is to develop a general strategy that makes an optimal use of the available resources. We start by discussing I/O requirements and later address the issue of allocating pixel computations among the nodes.

The retrieval of global BRDF requires extensive handling of large amounts of data residing in external storage (about 27 GBytes). We seek to achieve an efficient layout of the input imagery on the available disks and an efficient mapping of the computation across the available processors in such a way that (1) the total I/O time is minimized and (2) the computational loads are balanced among the nodes.

As stated earlier, the input consists of four years of PAL 10-day composite data, 1983 through 1986. The initial collection of input files is illustrated in Figure 2. Our input can be viewed as an array Data[Year][Month][Period][Layer][Row][Column], where we have 4 years, 12 months per year, 3 periods per month, 9 layers per period and the global pixels given by 2168 rows and 5004 columns. The 9 layers account for 17 bytes for each pixel. For example, on our multiprocessor platform that consists of 16-processor IBM SP2, the disk array on a node will hold 9 10-day composites and will have 81 images files, as shown in Figure 3. The image files can be accessed by giving the index[Year][Month][Period][Layer].

If we use one index "Time" to refer to (Year, Month, Period), we can view our input as a 4-dimensional array, Data[Time][Layer][Row][Column]. The time will vary from 1 to 144 in our case. There are totally 1296 input image files and 27 GBytes of
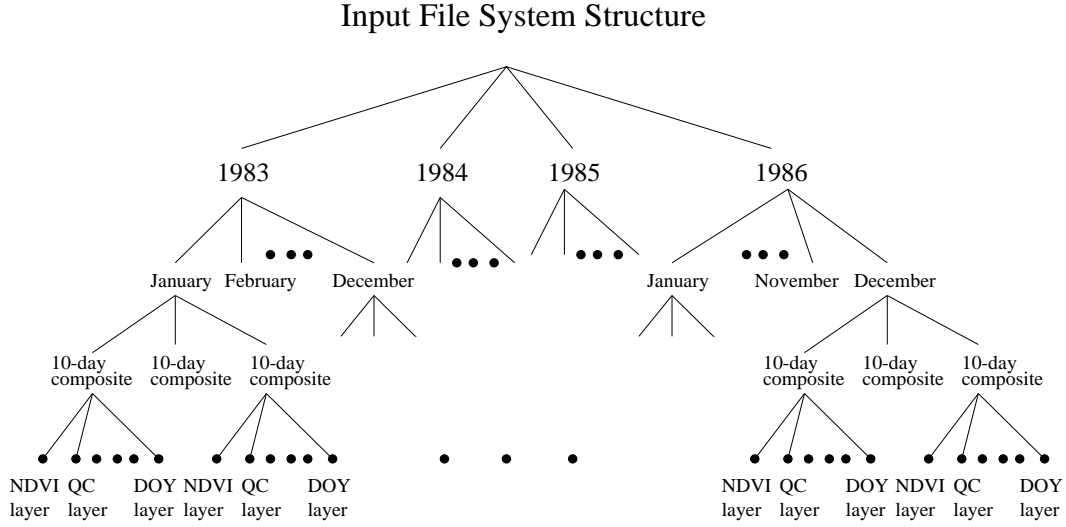
Input File System Structure

Figure 2: Structure of the input file system. Each year has 12 months, each month has 3 10-day composite, each 10-day composite has 9 layers and each layer is stored in a file
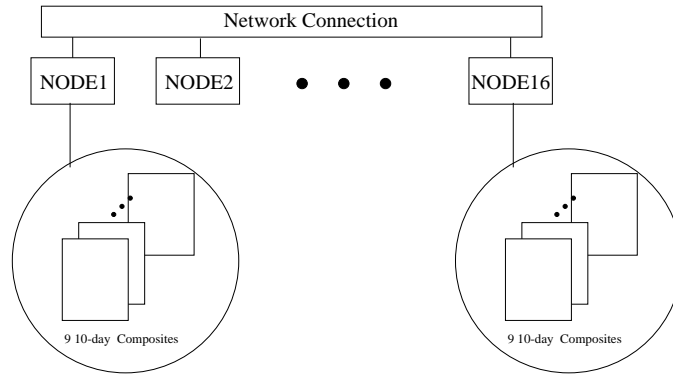

Figure 3: Initial distribution scheme of the input data among different nodes on a multiprocessor system. In this example, there are 16 nodes, and nine 10-day composite images are stored on the local disk of each node.

data ($= 5004 \times 2168 \times 17 \times 144$). This 4-dimensional array Data[Time][Layer][Row][Column] is distributed over the node according to the Time index. That is, if we have p nodes and the Time index ranges from 1 to T (assuming T is a multiple of p without loss of generality), then Data[$1 : \frac{T}{p}$][Layer][Row][Column] lies on the disks of node 1, Data[$\frac{T}{p} + 1 : \frac{2T}{p}$][Layer][Row][Column] lies on the disks of node 2,... Data[$\frac{(n-1)T}{p} + 1 : \frac{nT}{p}$][Layer][Row][Column] lies on the disks of node p.

In addition to the data, we also need the classmap information to classify a pixel either as a land pixel or as a water pixel as well as to give the class type of the surface. This information consists of a global image with one byte per pixel, and hence the size of the classmap is about 11Mbytes. ClassMap[Row][Column] is stored on one node.

We will generate all the model coefficients, the standard error and the R^2 coefficient for each channel, as well as the mean NDVI, the NDVI standard deviation and the NDVI standard error. Each of the output generated will be a 32-bit floating point number for each pixel. Let N_c denote the number of coefficients in the model. Then we will produce $NumCoef = 2(N_c + 2) + 3$ floating images (44Mbytes each) and one unsigned short image output for number of points used in model fitting, which amounts to approximately 670 MBytes for modified Walthall's model, 1.0GBytes for Liang's temporal model and 590 MBytes for Rahman's non-linear model. We can view these outputs as a 3-dimensional array Out[NumCoef][Row]Column] and one Num[Row][Column] unsigned short image.

4.2   Data Redistribution and Computation Mappings

Given a p-processor platform, we implement our algorithm as follows. Using the classmap, we generate a land sea mask that describes the relative land position in the original image. This land sea map is then broadcast to all the nodes.

We then extract the land pixel data at each node using an intermediate data structure DateInter[Year][Month][LandPixel][Period][Layer]. That is, we start by eliminating the non-land pixels in the data, followed by saving the remaining pixels as shown in Figure 4. This phase is refered to as the **preprocessing** phase.

Next, we redistribute the land data evenly among the nodes. This results in approximately 380 MBytes of data per node for $p = 16$. Given the size of the data, we perform the redistribution iteratively as follows. We process $c \times p$ consecutive land pixels during each iteration such that the first c land pixels are shipped to the first node, the second c land pixels are shipped to the second node, and so on, where c is the maximum number of pixels that can fit into the main memory of each node. Hence each node will get all the [Year][Month][Period][Layer] information for its c land pixels, as illustrated in Figure 5. Here we use Massage Passing Interface (MPI) [28] collective communication primitive (MPI_Alltoall) to do the interprocessor communication in the land pixel redistribution. MPI is a library specification for message-passing, which
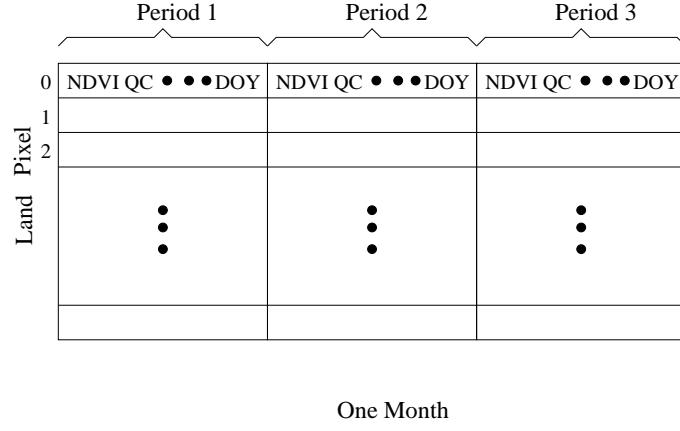
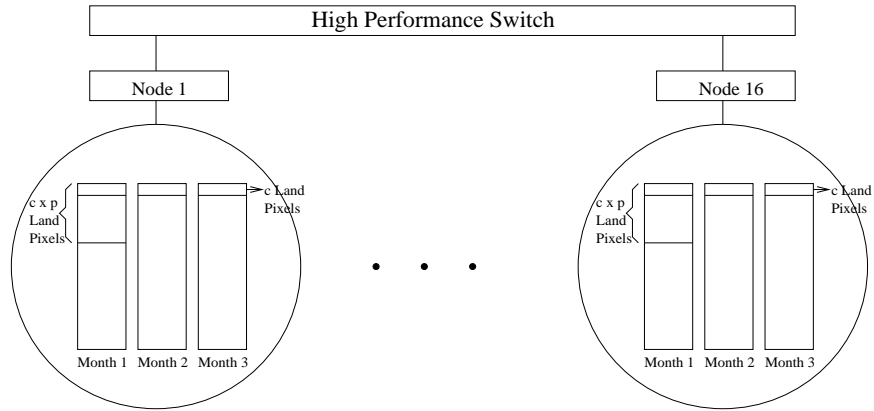Figure 4: Data structure used for land pixels after preprocessing on each node

Figure 5: After redistribution the top chunks of c land pixels will reside on node 1, the second c land pixels will reside on node 2, and so on.

is a paradigm used widely on distributed memory parallel machines. It is a standard proposed by a broadly based committee of vendors, implementors, and users [28].

We are now ready to perform the BRDF model fitting, for all the pixels on each node concurrently. We start by selecting the clear day data to form the curve fitting data set according to the CLAVR layer. We then compute the model coefficients, generate the model verification information and save it locally. After all the land pixels have been processed, we read back these coefficients from the temporary file one by one and collect them into one node by using MPI_Gather communication primitive. We reinsert the non-land information to make the output map back to the original globe image using land sea map generated in the first step.

4.3   Implementation and Performance Results

After preprocessing the input data and setting up the appropriate data structure for the land pixels, our algorithms consists of: (1) reading the land pixel data in chunks, (2) redistributing the land pixels among the multiprocessor nodes, (3) conditioning the land data, computing the model coefficients, and generating the model verification information, and (4) collecting all the coefficients to one node, remapping back to the original image, and generating the output. The time required to read the land pixel data (step (1)) is denoted by T_{input}. Interprocessor communication is required for the redistribution step (step (2)), whose corresponding time is denoted by T_{comm}. The time required to perform step (3) is denoted by T_{comp} (computation time). Finally, T_{output} refers to the time it takes to execute the fourth step for generating the output images on a single node.

Given that the loads are distributed equally among the processors, we expect T_{comp}, T_{input} to scale linearly with increased number of processors. We expect T_{comm} to scale almost linearly with increased number of processors since we are using balanced MPI collective communication primitives. We expect T_{output} to stay constant with increased number of nodes since all the output data is collected on one node.

Our testbed consists of a 16-node IBM SP2, each node is identically configured with one POWER2 processor, a 40MB/s bi-directional link for each processor to a multistage high performance switch, two fast-wide SCSI buses. Each SCSI bus has three 2.2 GB SCSI disks as shown in Figure 6.

A summary of the performance of our algorithms using this testbed is shown in Figure 7. Clearly the computation time (T_{comp}) and the land data input time (T_{input}) scale linearly with the number of processors. Also, the communication time T_{comm} scales almost linearly with the number of processors. On the other hand, T_{output} remains fairly constant relative to the number of nodes as we had expected. We should note that the preprocessing phase achieves a linear speedup over the number of processors.
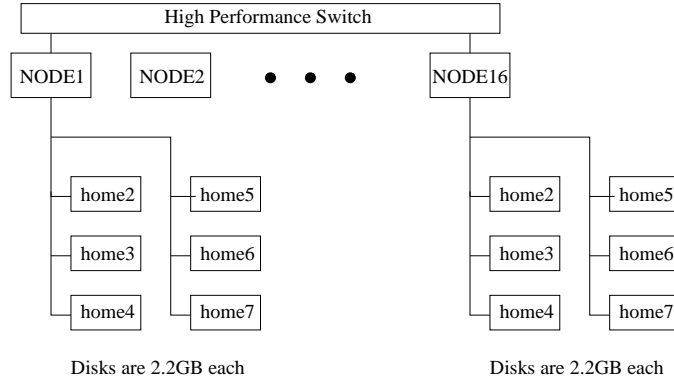
Figure 6: SP2 system configuration: Each node is an IBM POWER2 processor connected to a multistage high performance switch by a 40 MB/s bi-directional link. Each node has six 2.2 GB SCSI disks.

Regarding raw performance, on the 16-node SP2, the least squares fit computation achieves around 0.89 GFLOPS for the modified Walthall's model, and 0.91 GFLOPS for Liang's temporal mode. The nonlinear least squares fit achieves around 1.18 GFLOPS for Rahman's model. These numbers represent approximately 25% of the peak performance on our machine. The input bandwidth achieved is about 6.7 MB/s, the output bandwith achieved is about 6.0 MB/s, with the peak of either being 8 MB/s for each disk. The interprocessor communication bandwidth achieved is about 25 MB/s with a theoretical peak of 40 MB/s. These numbers clearly indicate the efficiency of our code in utilizing the available resources.

5   Comparison of Results from Different BRDF Models

As mentioned in Section 2, we generate the coefficients for each of the models corresponding to channels 1 and 2 of AVHRR, and standard errors between model predicted and actual reflectances. The coefficients describe the general shape of the BRDF for each pixel and could be potentially used to discriminate between different landcover types [18].

Consider for example, the coefficient a_3 for channels 1 and 2 respectively from the modified Walthall model for the third quarter (July-September) during $1983 - 86$ shown in Figure 8. The quantity a_3 is the nadir reflectance value in the individual AVHRR bands for this model. To our knowledge, this is the first time the coefficients of any BRDF model have been determined at a global scale. The spatial patterns of visible and near IR reflectances shown here are consistent with different land cover classes (e.g. [21]). Densely vegetated areas (e.g. central Africa, Brazil, Temperate
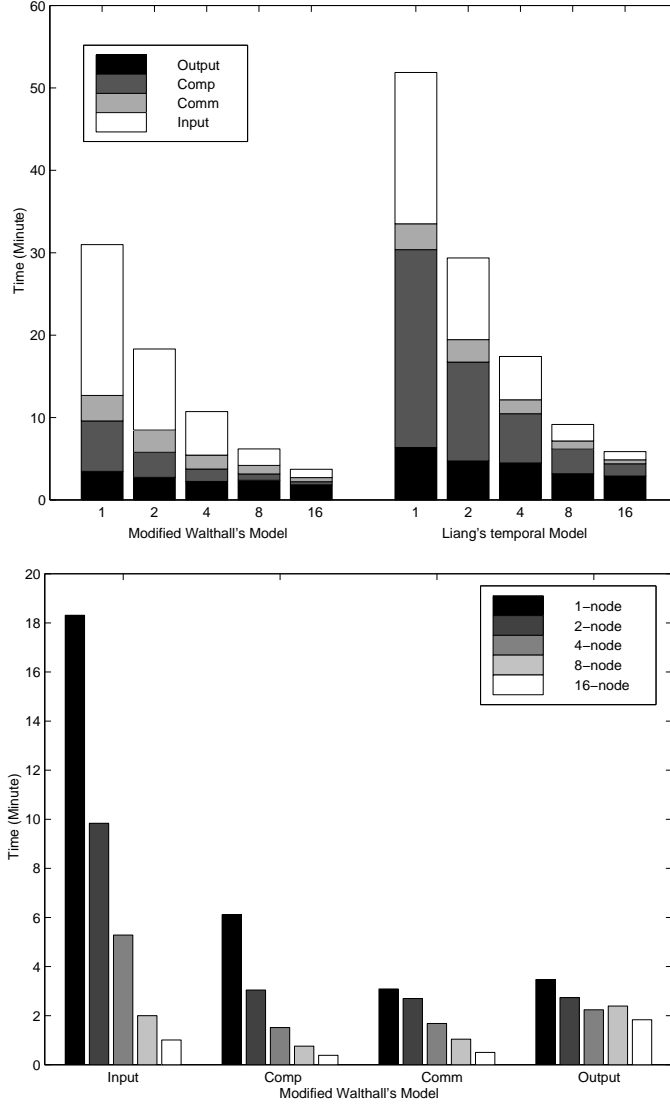
Figure 7: Timing of global BRDF retrieval from the four year PAL data set on a SP2 machine. The time spent on input, output, communication, and computation are shown seperately. Results are shown for different numbers of processors. The total time taken to run the Rahman's model is 150 minutes on 16 nodes, and is not shown here.

Coefficient a_3 for AVHRR channel 1 (modified Walthall's model)
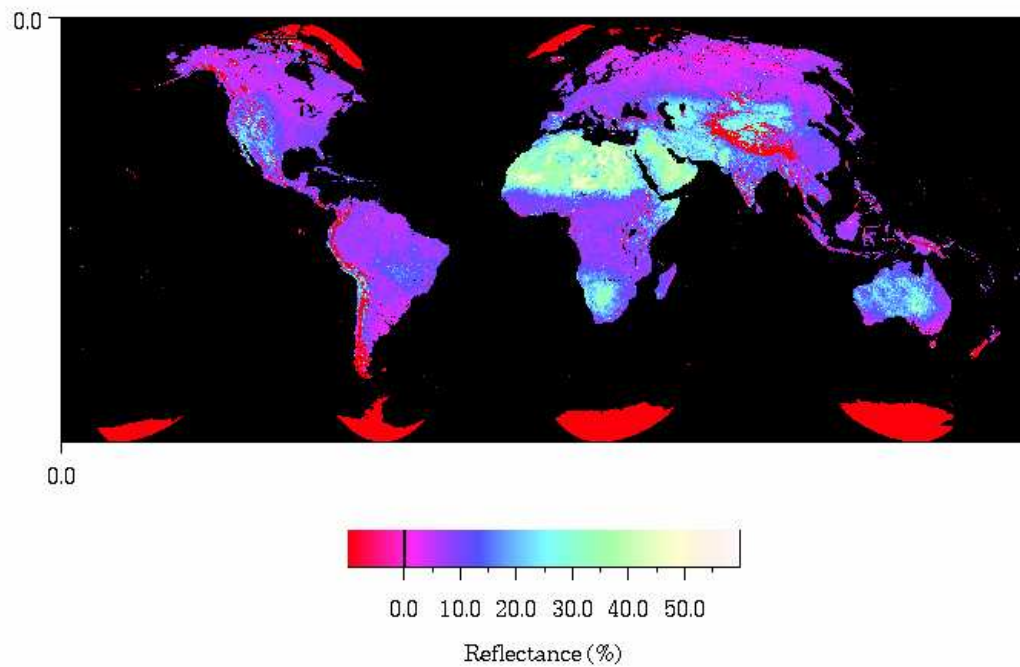
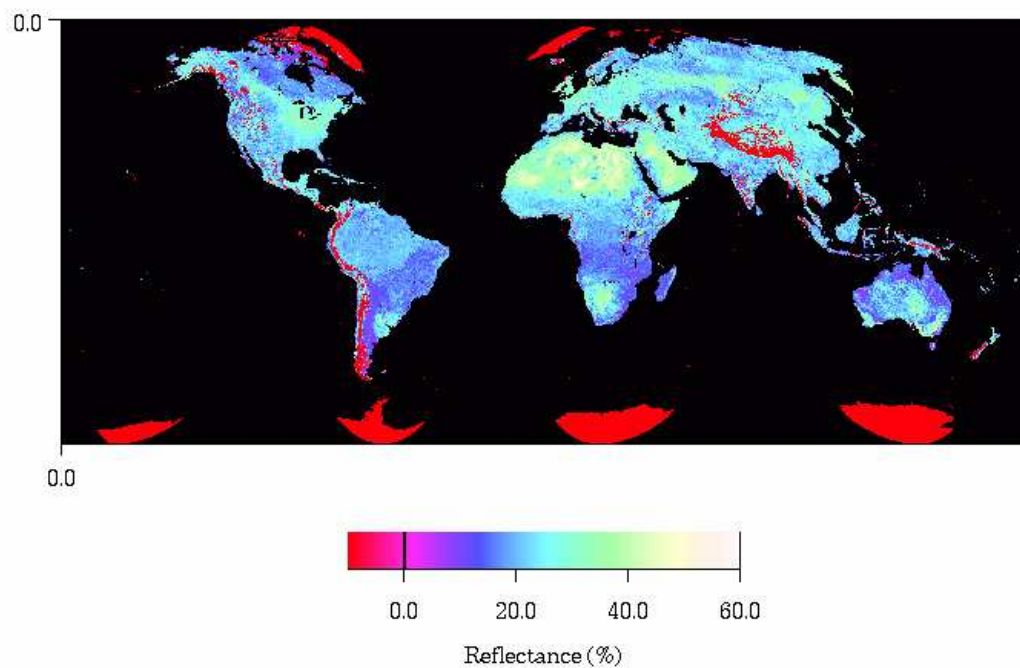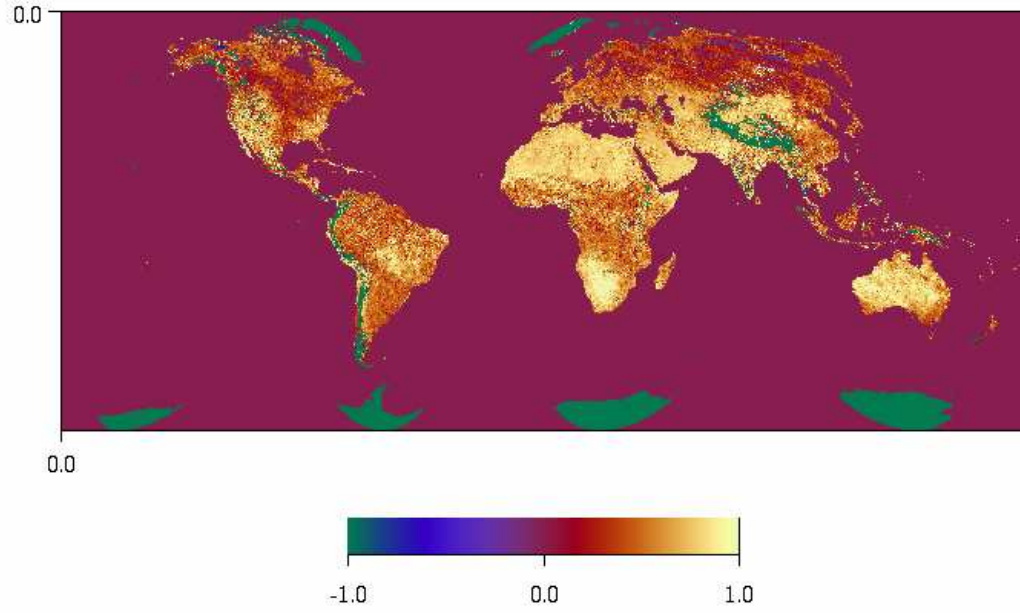Coefficient a_3 for AVHRR channel 2 (modified Walthall's model)

Figure 8: Coefficient a_3 from the modified Walthall's model for channels 1 and 2 of AVHRR for the time period July to September $(1983 - 1986)$. It represents nadir reflectance values for this model.

Coefficient k for AVHRR channel 1 (Rahman et al's model)

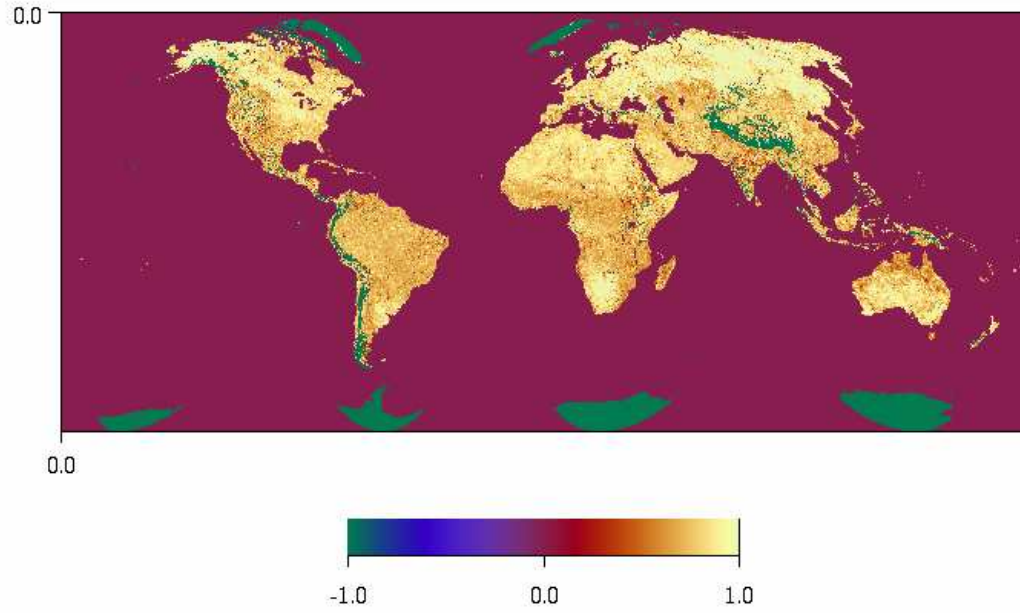Coefficient k for AVHRR channel 2 (Rahman et al's model)

Figure 9: Coefficient k from the Rahman et al's model for channels 1 and 2 of AVHRR for the time period July to September $(1983 - 1986)$. It describes the level of anisotropy of the surface. Lower values of k represent regions of high anisotropy.
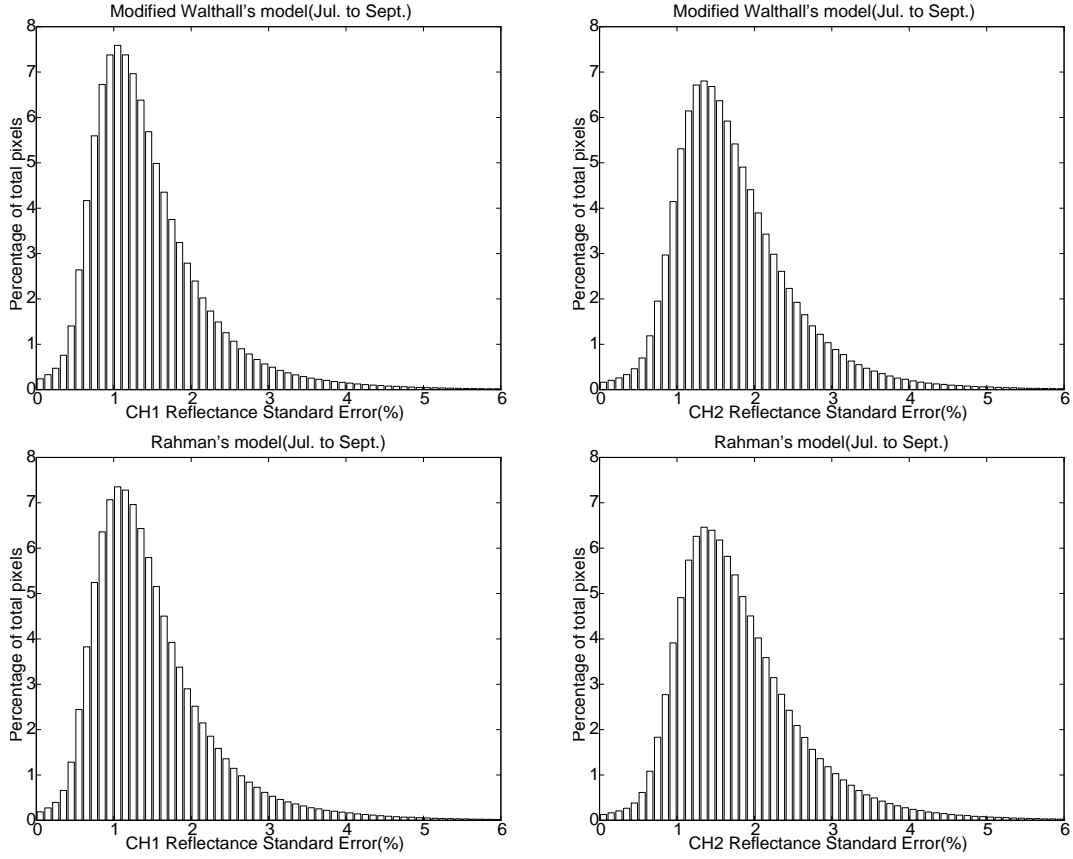
Figure 10: Comparison of standard errors in AVHRR channels 1 and 2 reflectances from the modified Walthall model and from Rahman et al's model during the third quarter (July to September) for the time period 1983-1986.

and Boreal forests in Asia and Europe) and agricultural regions (e.g. central USA) show high reflectances in channel 2 and very low reflectances in channel 1. Deserts on the other hand show high reflectances in both the bands (e.g. Sahara, central Australia, Kalahari). Insufficient data across the snow covered Himalayas, over the polar regions, and along the west coast of South America resulted in NULL values in these areas, which is due to the rejection of these pixels by CLAVR.

Figure 9 shows the parameter k for channels 1 and 2 of AVHRR for the Rahman et al's model. This parameter describes the variations in reflectance with view and illumination angles. Thus, it indicates the level of anisotropy of the surface [18]. It can be clearly seen from Figure 9 that the spatial variations of this parameter are closely related to the variations in landcover types. Lower values of k mean higher anisotropy. Vegetated areas show higher anisotropy in band 1 compared to band 2. Deserts, on the other hand, are less anisotropic in both bands compared to vegetated areas. Among the vegetated areas, high latitude deciduous forests have higher values

of k compared to tropical areas.

Comparison of the standard errors in channel 1 and 2 reflectances from the modified Walthall model and Rahman et al's iterative model shows that the magnitude of these errors is very similar in both models (Figure 10). However, the iterative model is computationally more expensive (150 minutes on a 16-node IBM SP2) than the modified Walthall model (15 minutes on a 16-node IBM SP2). Examination of the standard errors in reflectances from the other three quarters indicated that in general, both the models had higher errors in areas where there are pronounced variations in phenology during the time of observations.

Standard errors in channel 1 and 2 reflectances from the temporal model were larger in temperate regions of Asia, Europe and N. America, and also across the Sahel in Africa compared to other regions of the world (Figure 11). These errors could be due to large inter annual variations in surface conditions in these areas caused by changes in snow cover and rain fall in the higher latitudes and in the Sahel respectively.

6   Conclusion

We have demonstrated the feasibility of implementing both simple as well as complex algorithms to retrieve BRDF at global scales using high performance computing. An efficient method is presented here to handle the large data set involved. Our implementation optimizes I/O access time and efficiently balances computations across the nodes, which is achieved by redistributing the land pixels evenly across all the nodes.

Although the iterative model of Rahman et al. [18] was computationally more intensive compared to the modified Walthall model, results from the two algorithms were similar. The input data for these two models had to be partitioned into discrete time intervals to minimize the effects of surface phenology on BRDF retrieval. However, the temporal model negates the partitioning of input data based on variations in surface phenology. Errors from the temporal BRDF model were higher in temperate latitudes, and across the Sahel region in Africa compared to other locations, and this could be caused due to strong interannual variations in surface conditions in these two areas. The results from this study are unique, and are expected to provide valuable inputs into BRDF retrieval algorithms proposed for future Earth Observation System (EOS) instruments such as the Moderate Resolution Imaging Spectroradiometer (MODIS), and the Multiangle Imaging Spectroradiometer (MISR).

Acknowledgment

Channel 1 reflectance standard error (Liang's temporal model)

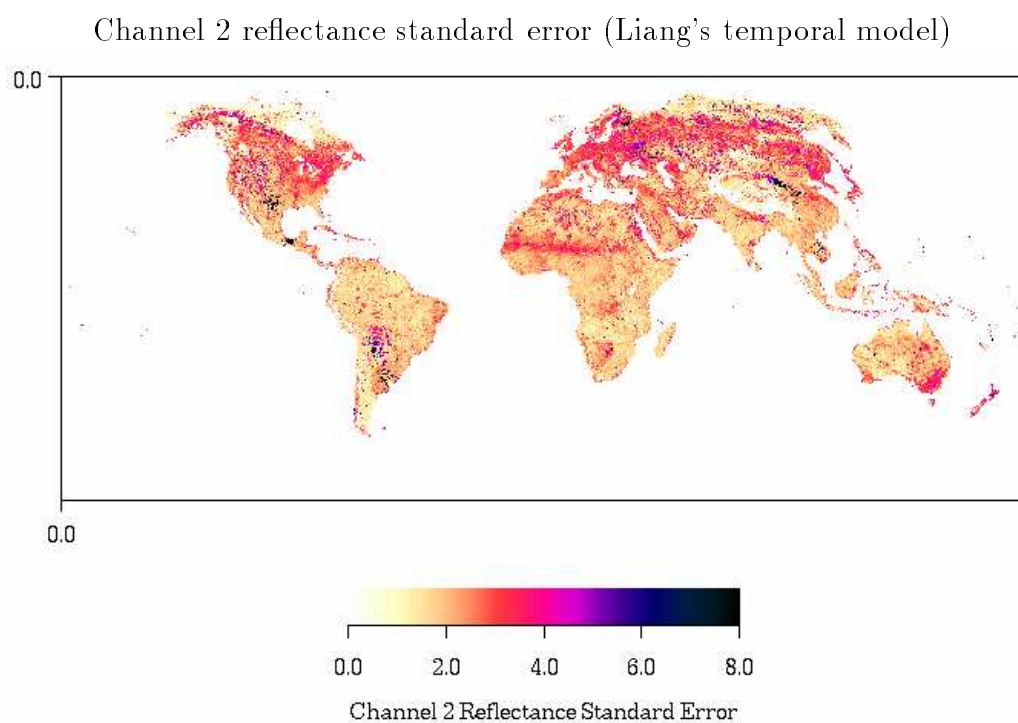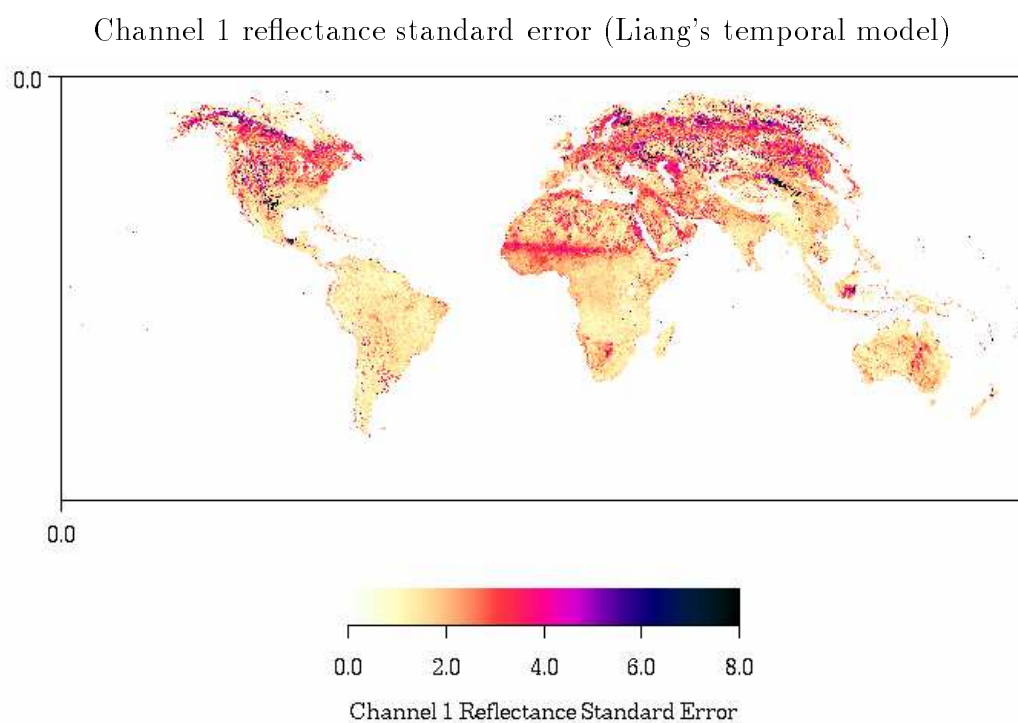Channel 2 reflectance standard error (Liang's temporal model)

Figure 11: AVHRR Channels 1 and 2 reflectance standard error for Liang's temporal model for the time period July to September ($1983 - 1986$)

Mitchell Murphy, Matt Beal, and Galen Wilkerson for their retrieving of the data and system support.

References

[1] Townshend, J.R.G., Justice, C.O., and Kalb, V.T., *Characterization and classification of South American land cover types using satellite data*, International Journal of Remote Sensing, 8, 1189-1207, 1987

[2] Pinker, R.T., Frouin, R. and Li, Z., *A review of satellite methods to derive surface shortwave irradiance*, Remote Sensing of Environment, 21, pp108-124, 1995.

[3] Tucker, C.J., Dregne, H.E. and Newcomb, W.W., *Expansion and contraction of the Sahara Desert from 1980 to 1990*, Science, 253, pp299-301, 1991

[4] Sellers, P.J., *Canopy reflectance, photo-synthesis, and transpiration*, International Journal of Remote Sensing, 6, pp1335-1371, 1985

[5] Prince, S.D., and Goward, S.N., *Global primary production: a remote sensing approach*, Journal of Biogeography, 22, pp815-835, 1995

[6] Nicodemus,F.E., Richmond, J.C., Hsia, J.J., Ginsberg, I.W., and Limperis, T. *Geometrical considerations and nomenclature for reflectance*, National Bureau of Standards, Report NBS MN-160, 1977

[7] Strahler A.H. and Muller J., *MODIS BRDF/Albedo Product: Algorithm Theoretical Nasis Document Version 3.2*, May 15, 1995,
http://spso.gsfc.nasa.gov/atbd/modis/atdmod09.html

[8] Ramanathan, V., *Scientific use of surface radiation budget data for climate studies*, NASA Reference Publication 1169, J.T. Suttles and G. Ohrings, Editors, 132pp.

[9] Cess, R.D., and Vulis, I.L., *Inferring surface-solar absorption from broadband satellite measurements*, Journal of Climate, 2, pp974-985, 1989.

[10] Li, X. and Strahler, A.H., *Geometric-optical bidirectional reflectance modeling of a conifer forest canopy*, IEEE Transactions on Geoscience and Remote Sensing, GE-24, pp906-919, 1986.

[11] Myneni, R.B., Ross, J., and Asrar, G., *A review on the theory of photon transport in leaf canopies*, Agric. For. Meteorol., 45, pp1-153, 1990

[12] Liang, S., and Strahler,A.H, *Calculation of the angular radiance distribution for a coupled atmosphere and canopy*, IEEE Trans. Geoscience and Remote Sensing, 31, pp.491-502, 1993

[13] Li, X., A H. Strahler and C. E. Woodcock, *A hybrid geometric optical-radiative transfer approach for modeling albedo and directional reflectance of discontinuous canopies*, IEEE Transactions on Geoscience and Remote Sensing, 33, pp466-480, 1995.

[14] Goel, N. S., Rozehnal, I., and Thompson, R. L., *A computer graphics based model for scattering from objects of arbitrary shapes in the optical region*, Remote Sensing of Environment, 36, pp73-104, 1991.

[15] Ross, J. K., Marshak, A. L., *Calculation of canopy bidirectional reflectance using the Monte Carlo method*, Remote Sensing of Environment, 24, pp213-225, 1989.

[16] Borel, C. C., Gerstl, S. A. W., and Powers, B. J., *The radiosity methods in optical remote sensing of structured 3-D surfaces*, Remote Sensing of Environment, 36, pp13-44, 1991.

[17] Nilson, T. and Kuusk, A. , *A reflectance model for the Homogeneous Plant Canopy and its Inversion*, Remote Sensing of Environment, 27, pp157-167, 1989

[18] Rahman, H., Verstraete, M.M. and Pinty, B., *Coupled surface-atmosphere reflectance model(CSAR), 1. Model description and inversion against synthetic data. 2. Semi-empirical surface model usable with NOAA AVHRR data*, Journal of Geophysical Research, 98, pp20779-20801, 1991

[19] Liang, S. and Townshend, J.R.G., *Angular signatures of NOAA/NASA Pathfinder AVHRR Land data and applications to land cover identification*, Proceedings of IGARSS, 1997.

[20] James, M.E. and Kalluri, S.N.V., The Pathfinder AVHRR land data set:An improved coarse resolution data set for terrestrial monitoring, International Journal of Remote Sensing, 15, pp3347-3363, 1994

[21] Defries, R.S. and Townshend, J.R.G., NDVI-derived land cover classifications at a global scale, International Journal of Remote Sensing, 15, pp3567-3586, 1994

[22] Clark, W.A.V. and Hosking, P.L., Statistical Methods for Geographers, John Wiley and Sons, New York, 1986

[23] Agbu, P.A., and M.E. James, *The NOAA/NASA Pathfinder AVHRR Land Data Set User's Manual Version 3.1*, The Goddard Distributed Active Archive Center, NASA, Goddard Space Flight Center, Greenbelt, Sept. 1994

[24] Stoer, J. and Burlirsch, R., *Introduction to Numerical Analysis*, Second Edition Springer-Verlag New York, Inc. 1993

[25] Golub G.H. and Van Loan C.F., *Matrix Computations*, The Johns Hopkins University Press, Baltimore, Maryland, 1983

[26] Brent R.P., *Algorithms for Minimization without Derivatives*, Prentice-Hall Inc., Englewood Cliffs, New Jersey, 1973

[27] Press W.H., Teukolsky S.A., Vetterling W.T. and Flannery B.P., *Numerical Recipes in C*, Second Edition, Cambridge University Press, 1992

[28] Message Passing Interface Forum, *MPI: A Message-Passing Interface Standard.* Version 1.1, June, 1995